ADVANCED MATERIALS
www.advmat.de

# Photosensitive Dielectric 2D Perovskite Based Photodetector for Dual Wavelength Demultiplexing

*Bao-Shi Qiao, Su-Yun Wang, Zhi-Hong Zhang, Zhen-Dong Lian, Zhi-Yao Zheng, Zhi-Peng Wei, Lin Li, Kar Wei Ng,* Shuang-Peng Wang,* and Zhi-Bo Liu**

**Stacked 2D perovskites provide more possibilities for next generation photodetector with more new features. Compared with its excellent optoelectronic properties, the good dielectric performance of metal halide perovskite rarely comes into notice. Here, a bifunctional perovskite based photovoltaic detector capable of two wavelength demultiplexing is demonstrated. In the Black Phosphorus/Perovskite/$MoS_2$ structured photodetector, the comprehensive utilization of the photosensitive and dielectric properties of 2D perovskite allows the device to work in different modes. The device shows normal continuous photoresponse under 405 nm, while it shows a transient spike response to visible light with longer wavelengths. The linear dynamic range, rise/decay time, and self-powered responsivity under 405 nm can reach 100, 38 µs/50 µs, and 17.7 mA $W^{-1}$, respectively. It is demonstrated that the transient spike photocurrent with long wavelength exposure is related to the illumination intensity and can coexist with normal photoresponse. Two waveband-dependent signals can be identified and used to reflect more information simultaneously. This work provides a new strategy for multispectral detection and demultiplexing, which can be used to improve data transfer rates and encrypted communications. This work mode can inspire more multispectral photodetectors with different stacked 2D materials, especially to the optoelectronic application of the wide bandgap, high dielectric photosensitive materials.**

## 1. Introduction

Metal-halid Perovskite materials have shown incredible performance in many optoelectronic applications in the past ten years.[1–2] For example, the highest certified power conversion efficiency of perovskite-based solar cells has reached 25.7%,[3–4] high-performance field effect transistor is realized by 2D perovskite oxides,[5] and the external quantum efficiency of perovskite light-emitting diodes has exceeded 20%.[6–7] These results demonstrate numerous outstanding advantages of perovskite, such as the large adsorption coefficient, long carrier lifetime, colossal permittivity, and high defect tolerance.[8–10] As an important optoelectronic building block, photodetectors are the core components in imaging, communication, and detection/alarm system, acting as the eye of machines.[11–12] Recently, perovskite-based photodetectors show huge prospects for their adjustable energy band gap, high sensitivity, and low-cost material synthesis and device fabrication.[13–14] In particular, perovskite-based photovoltaic detectors show higher linear dynamic range (LDR) than Si detectors in many reported works.[15–17] Other parameters like detectivity, responsivity, response time, and noise also show promising outlooks, although there is still room for improvements before their practical applications.[18]

Among all perovskite-based photodetectors, heterojunction structure is widely adopted due to the controllable depletion region, transparent transport layer, and short charge transit time, which are crucial for realizing high-performance photodetectors.[19] More advantageously, the feasibility to fabricate

B.-S. Qiao, Z.-H. Zhang, Z.-D. Lian, K. W. Ng, S.-P. Wang
Institute of Applied Physics and Materials Engineering
University of Macau
Macao SAR 999078, P. R. China
E-mail: billyng@um.edu.mo; spwang@um.edu.mo

S.-Y. Wang, Z.-B. Liu
The Key Laboratory of Weak Light Nonlinear Photonics
Ministry of Education
School of Physics and Teda Applied Physics Institute
Nankai University
Tianjin 300071, P. R. China
E-mail: liuzb@nankai.edu.cn

The ORCID identification number(s) for the author(s) of this article can be found under https://doi.org/10.1002/adma.202300632.

DOI: 10.1002/adma.202300632

Z.-H. Zhang, Z.-P. Wei
State Key Laboratory of High Power Semiconductor Lasers
Changchun University of Science and Technology
Changchun 130022, P. R. China

Z.-Y. Zheng
State Key Laboratory of Luminescence and Applications
Changchun Institute of Optics
Fine Mechanics and Physics
Chinese Academy of Sciences
No. 3888 Dongnanhu Road, Changchun 130033, P. R. China

L. Li
Key Laboratory for Photonic and Electronic Bandgap Materials
Ministry of Education
School of Physics & Electron Engineering
Harbin Normal University
Harbin 150025, P. R. China

 

heterojunction photodetector is enriched with the development of stacked 2D materials.[20] On the one hand, the mismatch of crystal lattice has little effect and a clear smooth interface can be obtained easily for the stacked structure. On the other hand, the stacking of low dimension materials can give rise to more and better unexpected properties.[21] Fu et al. fabricated a 2D perovskite-based photodetector with $MoS_2$ as the electron transport layer. Compared with the pure 2D perovskite-based device, the responsivity improved by more than 6 orders of magnitude.[22] Wang et al. reported an ultrahigh photo/dark current ratio (>$10^7$) device based on perovskite/black phosphorus (BP)/$MoS_2$ structure,[23] which demonstrates the potential of photodetector by stacked 2D materials and perovskite. Many reports have shown the superiority of perovskite-sandwiched structures through high performance.[24–25] However, perovskite-based detectors mostly take advantage of their high absorption coefficients only.[26–27] As an important feature of 2D materials, newfangled properties have attracted little attention in the stacked perovskite photodetectors. In particular, dielectric properties, a major property of perovskite materials, have not been widely studied and harnessed in optoelectronic devices.[28]

In this work, the dielectric property of large bandgap perovskite material is employed to realize detection capabilities different from the traditional photosensitive mode, and a dual-wavelength demultiplexer is achieved on a $MoS_2$/2D perovskite/BP structure photodetector. Here, the 2D perovskite synthesized through large cation spacers n-butylammonium (BA) acts as both the photosensitive material and dielectric layer, while the $MoS_2$ and BP layers are used as electron- and hole-transport layers, respectively. In addition, the $MoS_2$ layer is also active to the photons with energy ranging between the $MoS_2$ and perovskite band gaps. Based on the two properties, the perovskite-based device exhibits two radically different response modes towards various light wavelengths. Under short wavelength radiation (405-nm here), the perovskite layer serves as the active layer and the photodetector shows satisfactory performance including a high LDR of 100, fast rise/decay time of 38 µs/50 µs, and responsivity of 17.7 mA $W^{-1}$ at 0 V. When the device is placed under long wavelength illumination (650 nm here), electron-hole pairs can rarely be generated in the perovskite layer from the sub-bandgap light excitation such that the perovskite layer predominantly acts as a dielectric layer. Meanwhile, the photogenerated electrons and holes in the $MoS_2$ layer cannot pass through the high potential barrier with perovskite. Consequently, the device becomes a capacitor which stores the photogenerated carriers and the transient movement of the charges through the external circuit gives rise to a transient spike photocurrent. Furthermore, the integrated current intensity (charge accumulation) increases monotonically with the illumination intensity. Wavelength-multiplexed optical signals can therefore be detected with one single photovoltaic detector by simultaneously recognizing the transient spike response and normal continuous response. Compared with previously reported multispectral detectors achieved with voltage modulating, bidirectional photocurrent distinguishing, and afterglow tracking,[29–33] we provide a novel strategy to identify the illumination wavelengths based on the bi-functional 2D perovskite. Using the method, a dual-band optical parallel communication with two-wavelength demultiplexing is demonstrated. With the abundant choices of 2D materials and flexibility in the stacking scheme, the dielectric photosensitive materials are expected to realize more customized multispectral photodetectors.

## 2. Results and Discussions

Solution-grown $(BA)_2PbBr_4$ crystal is used in this work. The X-ray diffraction (XRD) pattern (Figure S1, Supporting Information) indicates the excellent quality of the 2D perovskite material. The $MoS_2/(BA)_2PbBr_4$/BP heterojunction is constructed by stacking the mechanically exfoliated few-layer $MoS_2$, $(BA)_2PbBr_4$, and BP onto a $Si/SiO_2$ substrate successively (**Figure 1**a). The area of the stacked region is ≈140 µm$^2$. Under light illumination, the photogenerated electrons and holes are drifted to $MoS_2$ and BP, respectively. The quality of the stacking layers is confirmed by photoluminescence (PL) and absorption spectra (Figure S2, Supporting Information) in which we can see the absorption edges of 2D perovskite and $MoS_2$ are at 420 nm and 680 nm, respectively. Raman spectra taken at four different positions of the layer stack are used to distinguish the materials and vibrational energy of the bonds in the corresponding regions (Figure 1b). Spectra I and III show the mixed scattering peaks of BP/Si and $MoS_2$/Si. Whereas the strongest Raman peak in II corresponds to the Si substrate, weak Raman peaks of $(BA)_2PbBr_4$ appear in the range from 50 to 100 nm.[34] Raman spectrum IV taken from the stacked region contains all the characteristic peaks of spectra I–III. It can be found no new chemical bond was created during the stacking process as no new scattering peaks occur. The scanning electron microscope (SEM) image (Figure 1c) shows the smooth surfaces of these 2D materials, while the energy-dispersive X-ray spectroscopy (EDS) mapping (Figure 1d–f) shows the clear boundaries among BP, $MoS_2$, and perovskite, which are beneficial for efficient carrier transfer and low reverse leakage current. High-resolution transmission electron microscopy (TEM) is used to characterize the ultrathin cross-section of the device (Figure S3, Supporting Information). The images and associated element distributions demonstrate that the thickness of BP, $(BA)_2PbBr_4$, and $MoS_2$ are ≈3 nm, 43 nm, and 27 nm, respectively. Although the structure of $(BA)_2PbBr_4$ is hard to be observed due to amorphization by the high-energy electrons, the layered lattices of BP and $MoS_2$ can be seen clearly in the high-resolution TEM images.

For electrical testing, gold electrodes are fabricated onto the $MoS_2$ and BP layers, respectively. The contact characteristics are analyzed with the *I*–*V* curves of metal-semiconductor-metal structures (Figure S4, Supporting Information). Due to the high carrier densities of $MoS_2$ and BP, Au electrodes can achieve good Ohmic contacts with a narrow depletion region and large tunneling current regardless of their work functions.[35–37]

The fabricated device exhibits a low dark current in typical photovoltaic characteristics measurement (**Figure 2**a), and a slight zero-point drift in dark is observed due to the charge and discharge of the capacitor during the measurement process. Under 405-nm illumination, photogenerated carriers are accelerated by the built-in electric field to form drift current, making

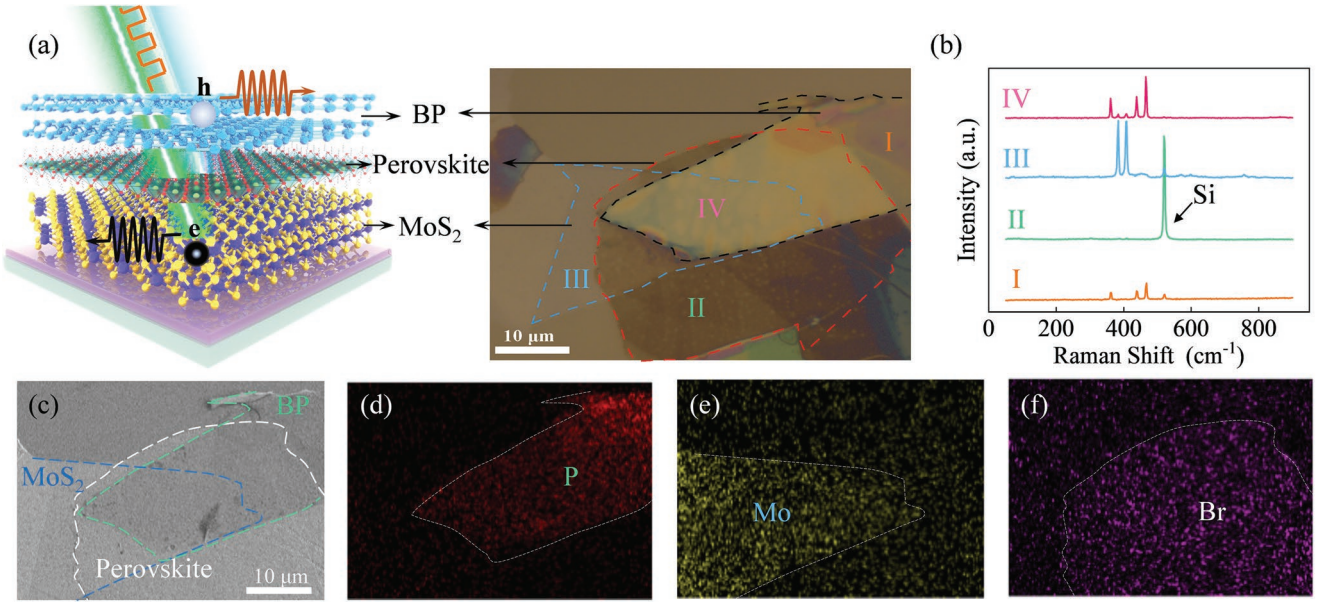


**Figure 1.** a) The diagram and optical microscope photographs of the device. b) The Raman spectra with exciting different positions (point I to IV in Figure 1a). c–f) SEM images and the corresponding EDS mapping of $MoS_2/(BA)_2PbBr_4$/BP device.

the device a photovoltaic cell, which leads to a larger zero-point drift in the *I–V* curves. With increasing illumination intensity, the short-circuit current (Figure 2b) and open-circuit voltage (Figure S6, Supporting Information) increase gradually, and the linear correlation between the short-current photocurrent and light intensity covers 5 orders of magnitude, which suggests a wide LDR of 100 dB according to Formula 1.[38]

$$\mathrm{LDR} = 20\log\frac{P_t}{P_b} \tag{1}$$

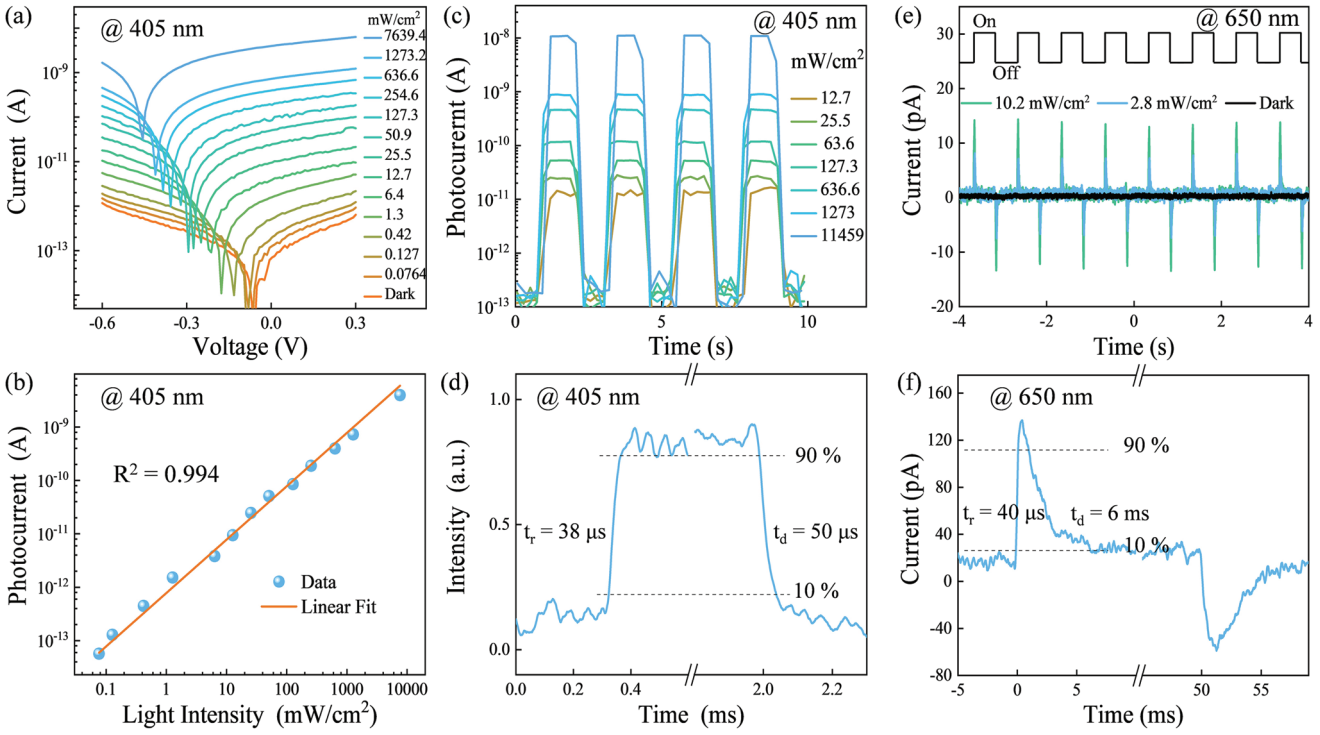


**Figure 2.** a) The *I–V* curves of $MoS_2/(BA)_2PbBr_4$/BP device under 405-nm illumination with different intensities. b) Photocurrents change with 405-nm illumination intensity at 0 V. c) The *I–t* curves and d) The time-resolved response signal of the device under 405-nm illumination, which are obtained from semiconductor analyzer and oscilloscope, respectively. e) The high-resolution *I–t* curves and f) the time-resolved response signal under 650-nm illumination.

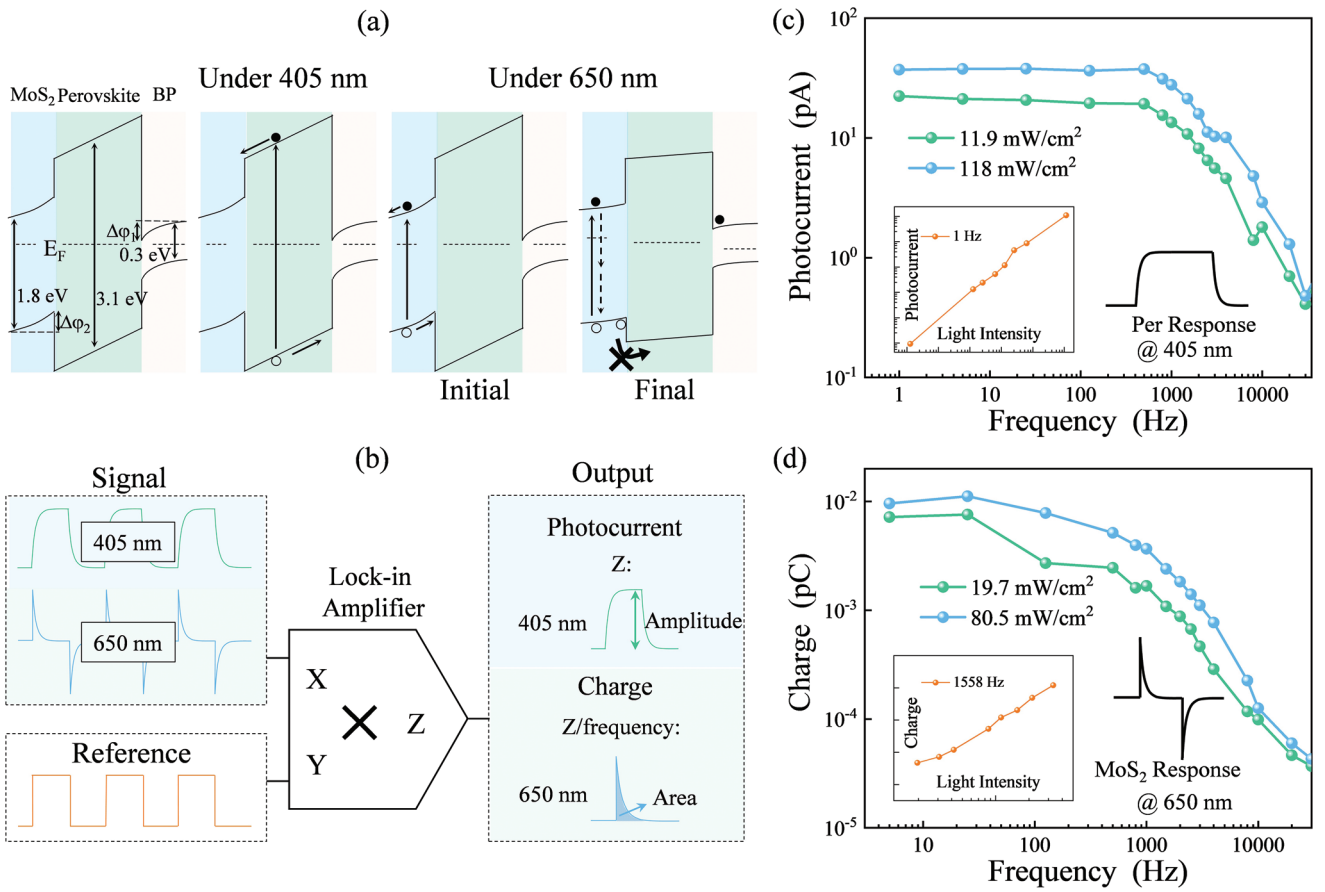


**Figure 3.** a) The diagram of the energy band in dark and under different illumination. b) The schematic of current and charge signals obtained from the lock-in amplifier. c) The photocurrent at 1 Hz changes with a 405-nm illumination frequency. The inset shows the photocurrent changing with illumination intensity. d) The charge changes with 650-nm illumination. The inset shows the charge at 1558 Hz changing with illumination intensity.

where the $P_t$ and $P_b$ are the upper and lower limits of light intensity at which the device has constant responsivity. Notably, this value is better than most 2D photodetectors.[39–41] In fact, due to the photogating effect, most of the low-dimensionality photodetectors cannot even keep linear dynamics.[42–43] Further, from Figure S6 (Supporting Information), it can be found the open-circuit voltage ($V_{OC}$) increases linearly with the logarithm of illumination intensity, suggesting the device is a nice photovoltaic detector. The current variation with illumination on/off measured by a semiconductor analyzer (Figure 2c) shows that the device exhibits stable photocurrent and excellent repeatability. To obtain the rise/decay time accurately, Figure 2d shows the time-resolved photocurrent obtained from an oscilloscope. The rise/decay time is 38 µs/50 µs, which can be considered pretty decent among the reported perovskite photodetectors.[12,15,44–46]

Besides the normal response to 405 nm illumination, as a result of the dielectric property in 2D perovskite, the device shows a miracle transient spike response towards long-wavelength illumination (Figure 2e). A stable and light intensity-related transient spike current can be observed when the device is operated under 650 nm illumination. Figure 2f exhibits the time-dependent parameters. Upon 650 nm illumination, the device current increases to the maximum value in 40 µs, and then decays to 10% within 6 ms. Such a spike can also be observed when removing the 650 nm illumination. These transient spike currents are commonly related to the pyro-phototronic effect, piezo-phototronic effect, and capacitive effect as reported.[47–48] Considering the small area of the ultrathin 2D perovskite, atomic force microscopy (AFM) and Kelvin probe force microscopy (KPFM) are applied to study the mechanism, as shown in Figure S7 (Supporting Information). The thickness of BP and perovskite are ≈30 nm and ≈40 nm respectively. The $MoS_2$ layer is only ≈3 nm thick, which is hard to be seen under a relatively large magnification. KPFM shows the surface potential of the 2D perovskite layer is 120 meV higher than the BP layer and 200 meV lower than the $MoS_2$ layer. The surface potential is related to the difference between the sample and the probe, which is usually used to study the difference in the Fermi levels.[49–50] That means the BP/perovskite/$MoS_2$ heterojunction exhibits a p-i-n-like energy band characteristic.

Based on the Fermi level difference and the known bandgaps of the layers, the dielectric property of 2D perovskite is deemed to lead to the spike response considering the wavelength selectivity, and the related schematic diagrams of the energy band alignments are drawn in **Figure 3**a. When the device is placed in the dark, because of the potential difference, a built-in electric field will be generated and tilt the energy band. Upon 405 nm

illumination, the perovskite layer plays the role of active material, and the device works as a normal photovoltaic detector. The electrons and holes generated in perovskite by light radiation are driven to $MoS_2$ and BP by the built-in electric field, respectively. Under 650 nm radiation, only the $MoS_2$ layer is excited, and perovskite acts as a dielectric layer to block the photogenerated carriers. The photogenerated electrons-holes will cause a large drift current and be probed in the external circuits at the initial state. At the same time, the photogenerated holes move to and accumulate at the interface between $MoS_2$ and 2D perovskite due to the curved energy band. With the accumulation of more and more holes, the net built-in electric field is gradually weakened and thus the energy band bending will be flattened out, which reduces the drift current. Due to the inherent capacitance of the 40-nm thick 2D perovskite layer, electrons gathered at the interface of BP and 2D perovskite owing to the Coulomb force. Namely, the "capacitance" is charged and the photocurrent disappears gradually. Similarly, the diffusion current will dominate upon a reduction in the drift current when turning off the 650 nm radiation, which will lead to a peak in the reverse pulse current as well. Remarkably, our device can work in both photovoltaic and capacitive modes at the time, and the signals can be measured simultaneously using a lock-in amplifier as illustrated in the schematic diagram shown in Figure 3b. While 405 nm illumination generates continuous photocurrent as the output signal, 650-nm illumination induces transient current pulses and current integration (charge) is used to define the signal intensity, which is obtained through the measurement of the photocurrent-time integral. Using this dual-mode detection strategy, the frequency responses of these two response modes can be predicted as follows. Similar to other typical photodetectors, the photocurrent induced by 405-nm illumination will remain the same before the cutoff frequency and decrease with increasing light switching frequency after that. The reason for the reduction is that the current under illumination cannot rise to its max value because the device cannot keep up with the switching speed of illumination. For the 650-nm illumination, the measured charge within each current pulse will fall slightly with increasing light switching rate even before the cutoff frequency, which is due to the loss of integrating range at the tail of the current spike. After the cutoff, a decay similar to the photocurrent will be observed.

Both signals obtained from the lock-in amplifier display exactly as predicted (Figure 3c,d). With increasing chopper frequency (i.e., light switching frequency) of the 405-nm illumination, the output signal stays the same before the cutoff frequency (800 Hz), and then decreases as expected. The photocurrent versus light intensity obtained at 1 Hz is shown in the inset. A linear increase is observed, which is nearly identical to the curve shown in Figure 2b. It indicates the curve of signal-light intensity can be well collected by lock-in amplifier. Upon 650-nm illumination, the decreases of charge with increasing chopper frequency also meet the expectations well. The inset demonstrates that the charge increases linearly with the logarithm of light intensity. It indicates that the quantity of electric charge depends on the device's photovoltage, and the device could detect the 650-nm illumination well by the charge accumulation. For the mixed illumination of 405 nm and 650 nm, the average photocurrent versus frequency is shown in Figure S8 (Supporting Information). It can be found the curve can be divided into two parts. At low frequency (<100 Hz), the average photocurrent is mainly contributed by the 405 nm laser, while in high frequency region (>500 Hz), it shows strong dependance on 650-nm illumination. That indicates this photodetector have the ability to realize multi-wavelength measurement.

To further prove that the transient spike photocurrent indeed originates from the dielectric property of 2D perovskite, the photo responses of devices with different perovskite thicknesses (65 nm and 26 nm) are studied (see **Figure 4**a,b). The layouts of the devices are verified by optical microscope and AFM (Figure S9, Supporting Information). When reducing the thickness of 2D perovskite, the cutoff frequency under 405-nm and 650-nm illuminations become lower. It is because thinner 2D perovskite will lead to the larger RC time constant, thus resulting in a lower cutoff frequency. In addition, the signal intensities change contrarily with thickness under 405 nm and 650 nm illumination. Thinner perovskite means less photon absorption under 405 nm illumination and thus lower photocurrent output. At the same time, thinner perovskite also means higher capacitance and thus more charge can be stored in the device (see Figure 4b). Figure 4c shows that under 19.1 mW $cm^{-2}$ of 650 nm illumination and keeping the device area as consistent as possible, the stored charge increases linearly with the reciprocal thickness of 2D perovskite, clearly indicating that photoresponse is indeed closely correlated with the capacitance of the perovskite layer.

Finally, the origin of 650-nm light adsorption is studied. Transient spike photocurrent can be observed when 450-nm and 520-nm light is absorbed by $MoS_2$ (Figure S10, Supporting Information), while no signals can be obtained under 980-nm illumination. Therefore, $MoS_2$ layer is inferred to be responsible for this long wavelength light adsorption. Photocurrent spectra are measured to characterize the response origin further, using a monochromator with a light chopper and a 150 W xenon lamp. A standard commercial Si detector is used as the control group, and the corresponding photocurrent changes little with different frequencies as shown in Figure S11 (Supporting Information). For the photodetector based on ultrathin 2D perovskite, a narrow photocurrent peak at the blue band can be found when the chopper frequency is 10 Hz. The response spectrum is plotted in the inset of Figure 4d and shows almost no response toward long wavelengths. While a wide photocurrent envelope appears gradually at higher frequencies (Figure 4d). Figure S12 (Supporting Information) shows the photocurrent spectra of Au/$(BA)_2PbBr_4$/Au and Au/$MoS_2$/Au, which correspond well to the absorption spectrum in Figure S2 (Supporting Information). It can be inferred that the narrow response to blue light comes from 2D perovskite and the wide response range is resulting from $MoS_2$. To explain the increase in photocurrent envelope, Figure S13 (Supporting Information) is included to show the schematic diagram of the output of transient spike current in the lock-in amplifier. It can be found that a higher frequency will lead to a higher output due to the increased area of the signal, which corresponds to the increased current of the envelope in Figure 4d. Besides photocurrent, the responsivity could also be calculated by:[51]

$$R = \frac{I_{ph} - I_d}{Ps} \tag{2}$$

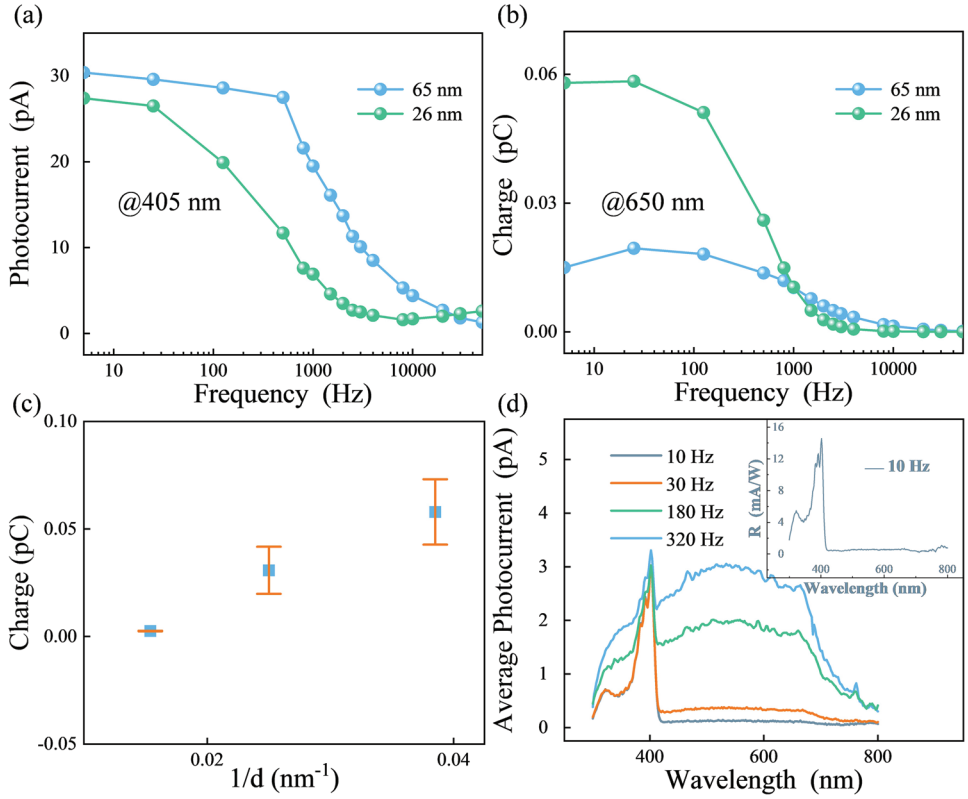


**Figure 4.** The signals with different thicknesses 2D perovskite versus chopper frequency under a) 405-nm illumination and b) 650-nm illumination. c) The charge under 19.1 mW cm$^{-2}$ 650-nm illumination versus thickness of 2D perovskite. d) The average photocurrent of $MoS_2/(BA)_2PbBr_4/BP$ photovoltaic detector, the inset shows the spectral responsivity of the device at 10 Hz. Other responsivity spectra at higher frequencies are not shown due to the nonlinear increase of transient spike photocurrent with light intensity.

where the $I_{ph}$ and $I_d$ are the photocurrent and dark current, $s$ is the effective area (140 μm$^2$). $P$ is the light power density, which can be calibrated through a standard Si photodetector. The photocurrent and responsivity of Si detector are 243 nA and 0.183 A W$^{-1}$ at 405 nm in this work, and the effective area is 1 mm$^2$. Thus, the calculated responsivity of 2D perovskite device is 17.7 mA W$^{-1}$ at 405 nm. Detectivity is one of the most important parameters to represent the weak-signal detection ability, which can be calculated by:

$$D^* = \frac{R\sqrt{s}}{\sqrt{2qI_d}} \tag{3}$$

where $q$ is the elementary charge, and the calculated $D^*$ is $1.5 \times 10^{11}$ Jones. Similar to the responsivity of 405 nm, the responsivity to long wavelength illumination can be defined by:

$$R = \frac{C_{ph}}{10\log(Ps)} \tag{4}$$

where $C_{ph}$ is the quantity of charge stored in the device under illumination, and $P_s$ is the received light power in the device with a unit of W. In this work, the responsivity is $-1.27 \times 10^{-16}$ C dB$_W^{-1}$ at 650 nm. It should be noted that this value is just used to calculate light power density by regression computation and not a value for comparison as the effect of area is nonlinear. Benefiting from the large absorption coefficient of 2D perovskite, our photodetectors exhibit decent performance in many aspects when compared with the reported stacked 2D materials-based photodetectors operating in self-powered mode (Summarized in **Table 1**). Beyond the absorption advantages of perovskite in stacked 2D photodetectors, the photosensitive dielectric 2D perovskite also promises the device two completely different operation modes, which enables the device to realize real-time waveband recognition. Such extraordinary functionality is enabled by the effective detection of the transient spike photocurrents, which were usually ignored as "jitter" current noise in previous photodetector studies.

As the photodetector can distinguish 405-nm and 650-nm illumination simultaneously, this device is expected to be used for two-wavelength demultiplexing in optical communication. **Figure 5**a shows the measurement schematic diagram. 405-nm and 650-nm lasers are used to send the messages "*IAPME UM*" and "*2D Material*", respectively. The received signals from an oscilloscope (as shown in the boxed spectrum in Figure 5a) show two clear response modes that correspond to the different signal sources. For the transient spike signals, the differential operation is used to amplify the signals, as shown in Figure 5b. The upward and downward spikes correspond to the rising and falling edges of the input optical signal, respectively. For the signals from the 405 nm laser, a smoothing operation was used to reduce the effects from transient spike signals. Using these signal processing techniques, both messages can be received and extracted at the same time. The above results indicate that

**Table 1.** Comparison of other stacked 2D materials-based photodetectors with our device.

| Device | $R$ [A W$^{-1}$] | $t_r/t_d$ [ms] | $D^*$ [Jones] | LDR | Waveband Recognition | Ref. |
|---|---|---|---|---|---|---|
| $In_2Se_3$/2D PVK[a)]/$MoTe_2$ | 0.288 | 0.73/0.62 | $1.2 \times 10^{12}$ | – | n | [24] |
| $MoS_2$/Gr/2D PVK | $10^5$ | 0.7/1.1 | $10^{15}$ | – | n | [40] |
| $WSe_2/Bi_2Te_3$ | 2100 | 0.18/0.21 | – | – | n | [52] |
| $MoTe_2/MoS_2$ | 0.322 | 25 | – | – | n | [53] |
| $PbSe_2/MoS_2$ | 42.1 | 74.5/93.1 | $8.2 \times 10^9$ | – | n | [54] |
| Gr/2D PVK/Gr | 0.46 | 0.49/0.54 | $1.2 \times 10^{13}$ | 122 | n | [55] |
| GaSe/$MoS_2$ | 0.05 | 50 | $10^{10}$ | 70 | n | [56] |
| InSe/Gr | 0.365 | 0.0002 | $1.3 \times 10^{13}$ | 40 | n | [57] |
| $ReS_2$/Au/$WSe_2$ | $10^{-5}$ | 20/15 | – | – | y | [58] |
| $MoS_2$/2D PVK/BP | 0.018 | 0.038/0.05 | $1.5 \times 10^{11}$ | 100 | real-time | this work |

[a)]PVK: Perovskite

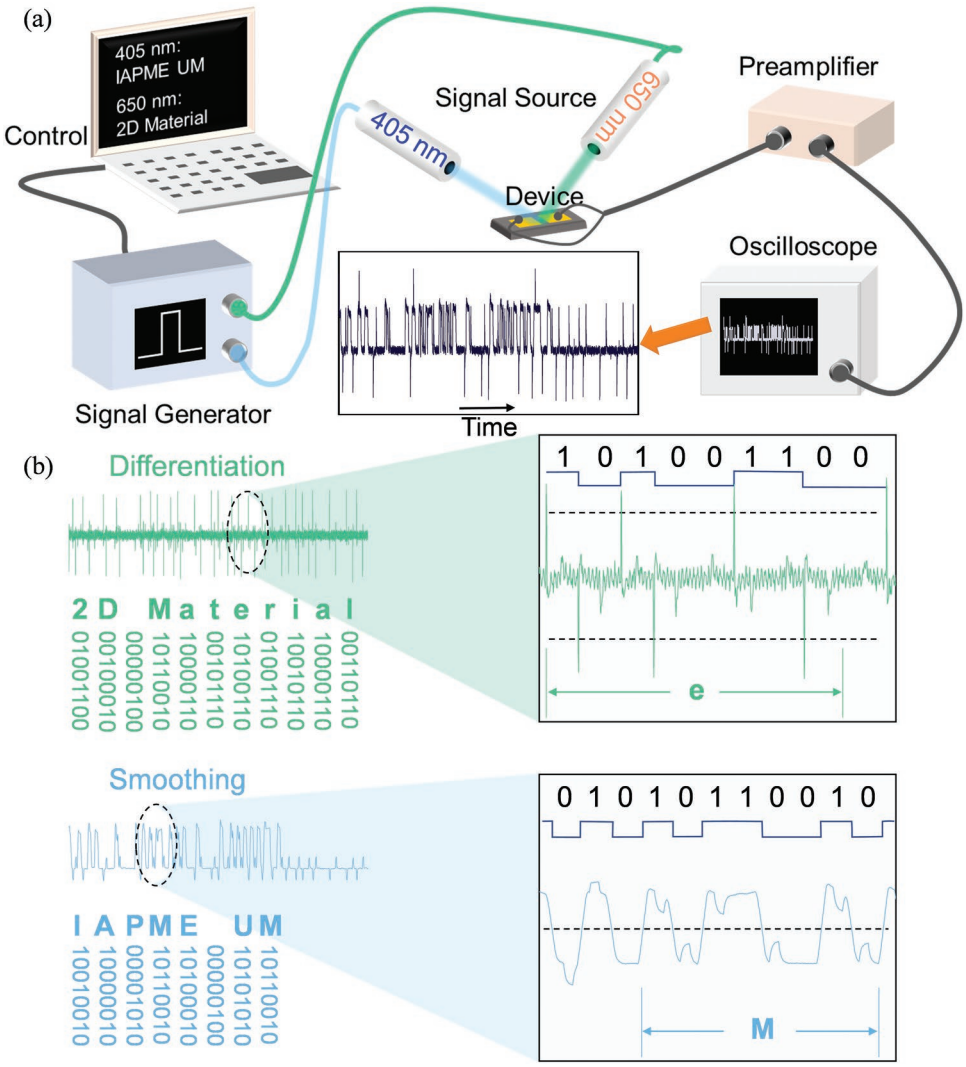


**Figure 5.** a) The diagram of optical communication. b) The differential calculus (corresponding to 650 nm) and smoothing (corresponding to 405 nm) of the received signal. The partial details are shown in right.

the single device can realize two-wavelength demultiplexing in parallel optical communication.

## 3. Conclusion

To sum up, a photovoltaic detector based on bi-functional 2D perovskite is fabricated, where $MoS_2$ and BP are used to collect electrons and holes, respectively. The device shows self-driven photodetection at 405 nm with a high LDR of 100, a fast rise/decay time of 38 µs/50 µs, and a responsivity of 17.7 mA $W^{-1}$. In addition, the fabricated device has a transient spike response to the illumination absorbed by $MoS_2$. The photosensitive properties of 2D perovskite and $MoS_2$, and the dielectric character of perovskite play key roles in this multi-functional device. And on this base, a two-wavelength parallel optical communication is realized with the device. This work exhibits an application strategy and the superiority of stacked 2D perovskite devices. With the great variety of stacked 2D materials, the results here are expected to stimulate more investigations and realizations of the customized multispectral photodetector and two-wavelength demultiplexing.

## 4. Experimental Section

The $(BA)_2PbBr_4$ crystals were synthesized by solution method. BABr precursor solution was prepared by mixing 494 µL BA (99.5%, MACKLIN) with 2.5 mL HBr (48 wt. %, Aladdin) solution in an ice-water bath. For the $PbBr_2$ solution, 563 mg PbO (99.99%, MACKLIN) was dissolved by 2.5 mL HBr (48 wt. %, Aladdin) and heated to 150 °C under magnetic stirring. Then BABr solution was added to the $PbBr_2$ solution with constant magnetic stirring until the solution is transparent. After that, stopped the stirring and cool the solution to room temperature at 1 °C $min^{-1}$. The white crystal will crystallize during the cooling process. Finally, the prepared perovskite was washed with dichloromethane and dried at 75 °C for 0.5 h before use.

The few-layer BP, $MoS_2$, and $(BA)_2PbBr_4$ were prepared by the mechanical exfoliation method using Scotch tape. BP and $(BA)_2PbBr_4$ were transferred onto the surface of polydimethylsiloxane, and the $MoS_2$ was exploited onto the surface of a $Si/SiO_2$ substrate. The high-quality few-layer samples were selected with an optical microscope. Finally, the few-layer $MoS_2$, $(BA)_2PbBr_4$, and BP were stacked together by the dry transfer method. All the procedure was accomplished in the $N_2$ atmosphere. Au (≈100 nm) electrodes were deposited onto the surfaces of BP and $MoS_2$, while a hard mask of 25-µm Au microwire was used to separate the electrodes. The schematic of the relevant fabrication process was shown in Figure S14 (Supporting Information).

Rigaku Smart Lab 9 kW system was used to characterize XRD spectra with Cu k$\alpha$ line ($\lambda \approx 1.54$ Å). SEM image and Energy-disperse X-ray spectroscopy (EDS) data were obtained from Zeiss Sigma. AFM and KPFM (Dimension Icon, Bruker, USA) were used to measure the height and surface potential of samples. TEM characterizations were performed on a Talos F200X, FEI microscope. The sample for TEM was prepared by a focused ion beam system (FIB, Zeiss Crossbeam 540 Gemini 2). The PL spectra were recorded under 325-nm excitation by a Confocal Laser Raman Spectrometer (LabRAM HR Evolution, HORIBA, Japan). Absorption spectra were measured by Acton SpectraPro SP-2750 with a self-built micro-optical system. The high-precision *I–V* and *I–t* curves were measured by a semiconductor analyzer (B1500A, Keysight, USA), and high-resolution *I–t* and time-resolved signals were obtained from Mixed Domain oscilloscope (MDO4054C, Tektronix, USA) with preamplifier (SR570, Stanford Research Systems, USA). The photocurrent spectra under different light wavelengths were measured from a response measurement system equipped with a monochromator (Zolix Instruments, China), a lock-in amplifier (SR830 Stanford Research Systems, USA), and a 150-W xenon lamp. The photocurrent versus frequency was obtained from the lock-in amplifier with the illumination of a frequency-adjustable laser. A waveform generator (DG4602 RIGOL, China) was used to provide dual-channel customized serial output, Mixed Domain oscilloscope (MDO4054C, Tektronix, USA) with a preamplifier (SR570, Stanford Research Systems, USA) were used to record the output signal from the photodetector.

## Supporting Information

Supporting Information is available from the Wiley Online Library or from the author.

## Acknowledgements

B.-S.Q. and S.-Y.W. contributed equally to this work. This work was supported by Science and Technology Development Fund from Macau SAR (File Nos. 0071/2019/AMJ, 0125/2018/A3, 0038/2019/A1, and 0052/2021/AGJ), Multi-Year Research Grants (MYRG2020-00207-IAPME, MYRG2022-00063-IAPME, and MYRG2019-00103-IAPME) from the University of Macau, and the Natural Science Foundation of China (Grant No. 12174207).

## Conflict of Interest

The authors declare no conflict of interest.

## Data Availability Statement

The data that support the findings of this study are available from the corresponding author upon reasonable request.

## Keywords

2D material, demultiplexer, dual-wavelength, perovskite, photovoltaic detector

Received: January 19, 2023
Revised: February 28, 2023
Published online: March 28, 2023

[1] Z. Zhang, P. Zheng, S. S. Yan, B. S. Qiao, K. W. Ng, H. C. Liu, S. P. Wang, Z. Wei, *Adv. Opt. Mater.* **2022**, *11*, 2201847.
[2] S.-S. Yan, Y. Ma, Y.-C. Kong, J.-Z. Jiang, X.-H. Xie, S.-C. Su, Z.-K. Tang, L. Shen, S.-P. Wang, K. W. Ng, *J. Mater. Chem. C* **2021**, *9*, 4771.
[3] Z. Li, X. Wang, Z. Wang, Z. Shao, L. Hao, Y. Rao, C. Chen, D. Liu, Q. Zhao, X. Sun, C. Gao, B. Zhang, X. Wang, L. Wang, G. Cui, S. Pang, *Nat. Commun.* **2022**, *13*, 4417.
[4] Y. Hou, E. Aydin, M. De Bastiani, C. Xiao, F. H. Isikgor, D.-J. Xue, B. Chen, H. Chen, B. Bahrami, A. H. Chowdhury, A. Johnston, S.-W. Baek, Z. Huang, M. Wei, Y. Dong, J. Troughton, R. Jalmood, A. J. Mirabelli, T. G. Allen, E. Van Kerschaver, M. I. Saidaminov, D. Baran, Q. Qiao, K. Zhu, S. De Wolf, E. H. Sargent, *Science* **2020**, *367*, 1135.

[5] W. Zhou, S. Zhang, H. Zeng, *Nat. Electron.* **2022**, *5*, 199.
[6] K. Lin, J. Xing, L. N. Quan, F. P. G. de Arquer, X. Gong, J. Lu, L. Xie, W. Zhao, D. Zhang, C. Yan, W. Li, X. Liu, Y. Lu, J. Kirman, E. H. Sargent, Q. Xiong, Z. Wei, *Nature* **2018**, *562*, 245.
[7] A. Fakharuddin, M. K. Gangishetty, M. Abdi-Jalebi, S.-H. Chin, A. R. bin Mohd Yusoff, D. N. Congreve, W. Tress, F. Deschler, M. Vasilopoulou, H. J. Bolink, *Nat. Electron.* **2022**, *5*, 203.
[8] T. Zhu, X. Gong, *InfoMat* **2021**, *3*, 1039.
[9] S. Yan, K. Wang, G. Xing, J. Xu, S. Su, Z. Tang, S. Wang, K. W. Ng, *ACS Appl. Mater. Interfaces* **2021**, *13*, 38458.
[10] H.-Y. Chen, W.-P. Bian, Y.-F. Wang, J. Yan, L. Li, H.-B. Wang, B.-S. Li, *Faguang Xuebao* **2019**, *40*, 1261.
[11] H. L. Loi, J. Cao, X. Guo, C. K. Liu, N. Wang, J. Song, G. Tang, Y. Zhu, F. Yan, *Adv. Sci.* **2020**, *7*, 2000776.
[12] L. Shen, Y. Fang, D. Wang, Y. Bai, Y. Deng, M. Wang, Y. Lu, J. Huang, *Adv. Mater.* **2016**, *28*, 10794.
[13] J. Wang, C. Fang, J. Ma, S. Wang, L. Jin, W. Li, D. Li, *ACS Nano* **2019**, *13*, 9473.
[14] Y. Xue, J. Yuan, J. Liu, S. Li, *Nanomaterials* **2018**, *8*, 591.
[15] C. Bao, Z. Chen, Y. Fang, H. Wei, Y. Deng, X. Xiao, L. Li, J. Huang, *Adv. Mater.* **2017**, *29*, 1703209.
[16] X. Feng, M. Tan, M. Li, H. Wei, B. Yang, *Nano Lett.* **2021**, *21*, 1500.
[17] C. Li, H. Wang, F. Wang, T. Li, M. Xu, H. Wang, Z. Wang, X. Zhan, W. Hu, L. Shen, *Light Sci Appl* **2020**, *9*, 31.
[18] C. Li, Y. Ma, Y. Xiao, L. Shen, L. Ding, *InfoMat* **2020**, *2*, 1247.
[19] C. Fang, H. Wang, Z. Shen, H. Shen, S. Wang, J. Ma, J. Wang, H. Luo, D. Li, *ACS Appl. Mater. Interfaces* **2019**, *11*, 8419.
[20] J. Ghosh, P. K. Giri, *J. Phys. Mater.* **2021**, *4*, 032008.
[21] K. Roy, M. Padmanabhan, S. Goswami, T. P. Sai, G. Ramalingam, S. Raghavan, A. Ghosh, *Nat. Nanotechnol.* **2013**, *8*, 826.
[22] Q. Fu, X. Wang, F. Liu, Y. Dong, Z. Liu, S. Zheng, A. Chaturvedi, J. Zhou, P. Hu, Z. Zhu, F. Bo, Y. Long, Z. Liu, *Small* **2019**, *15*, e1902890.
[23] L. Wang, X. Zou, J. Lin, J. Jiang, Y. Liu, X. Liu, X. Zhao, Y. F. Liu, J. C. Ho, L. Liao, *ACS Nano* **2019**, *13*, 4804.
[24] T. Yan, F. Liu, Y. Wang, J. Yang, C. Ding, Y. Cai, Z. Wu, X. Zhan, F. Wang, Y. Tian, J. He, Z. Wang, *Adv. Electron. Mater.* **2022**, *8*, 2101385.
[25] Y.-T. Li, L. Han, H. Liu, K. Sun, D. Luo, X.-L. Guo, D.-L. Yu, T.-L. Ren, *ACS Appl. Electron. Mater.* **2022**, *4*, 547.
[26] R. Ding, C. K. Liu, Z. Wu, F. Guo, S. Y. Pang, L. W. Wong, W. F. Io, S. Yuan, M. C. Wong, M. B. Jedrzejczyk, J. Zhao, F. Yan, J. Hao, *Nano Lett.* **2020**, *20*, 2747.
[27] X. Zhang, C. Ji, X. Liu, S. Wang, L. Li, Y. Peng, Y. Yao, M. Hong, J. Luo, *Adv. Opt. Mater.* **2020**, *8*, 2000311.
[28] M. J. Hong, L. Zhu, C. Chen, L. Tang, Y. H. Lin, W. Li, R. Johnson, S. Chattopadhyay, H. J. Snaith, C. Fang, J. G. Labram, *J. Am. Chem. Soc.* **2020**, *142*, 19799.
[29] D. Wang, X. Liu, Y. Kang, X. Wang, Y. Wu, S. Fang, H. Yu, M. H. Memon, H. Zhang, W. Hu, Z. Mi, L. Fu, H. Sun, S. Long, *Nat. Electron.* **2021**, *4*, 645.
[30] N. Ganesh, R. Shivanna, R. H. Friend, K. S. Narayan, *Nano Lett.* **2019**, *19*, 6577.
[31] Z. Lan, Y. Lei, W. K. E. Chan, S. Chen, D. Luo, F. Zhu, *Sci. Adv.* **2020**, *6*, eaaw8065.
[32] L. Li, H. Chen, Z. Fang, X. Meng, C. Zuo, M. Lv, Y. Tian, Y. Fang, Z. Xiao, C. Shan, Z. Xiao, Z. Jin, G. Shen, L. Shen, L. Ding, *Adv. Mater.* **2020**, *32*, 1907257.
[33] A. Kirch, T. Barschneider, T. Achenbach, F. Fries, M. Gmelch, R. Werberger, C. Guhrenz, A. Tomkeviciene, J. Benduhn, A. Eychmuller, K. Leo, S. Reineke, *Adv. Mater.* **2022**, *34*, 2205015.
[34] H. Li, Y. Qin, B. Shan, Y. Shen, F. Ersan, E. Soignard, C. Ataca, S. Tongay, *Adv. Mater.* **2020**, *32*, 1907364.
[35] A. T. Neal, H. Liu, J. J. Gu, P. D. Ye, *70th Device Research Conference*, University Park, PA, USA **2012**, pp. 65–66.
[36] J. Miao, S. Zhang, L. Cai, C. Wang, *Adv. Electron. Mater.* **2016**, *2*, 1500346.
[37] B. Radisavljevic, A. Radenovic, J. Brivio, V. Giacometti, A. Kis, *Nat. Nanotechnol.* **2011**, *6*, 147.
[38] Z. Ji, G. Cen, C. Su, Y. Liu, Z. Zhao, C. Zhao, W. Mai, *Adv. Opt. Mater.* **2020**, *8*, 2001436.
[39] T. Wang, D. Zheng, J. Zhang, J. Qiao, C. Min, X. Yuan, M. Somekh, F. Feng, *Adv. Func. Mater.* **2022**, *32*, 2208694.
[40] Y. Lu, X. Sun, H. Zhou, H. Lai, R. Liu, P. Liu, Y. Zhou, W. Xie, *Appl. Phys. Lett.* **2022**, *121*, 161104.
[41] Y. Zha, Y. Wang, Y. Sheng, X. Zhang, X. Shen, F. Xing, C. Liu, Y. Di, Y. Cheng, Z. Gan, *Appl. Phys. Lett.* **2022**, *121*, 191904.
[42] H. Fang, W. Hu, *Adv. Sci.* **2017**, *4*, 1700323.
[43] J. Yang, H. Kwak, Y. Lee, Y. S. Kang, M. H. Cho, J. H. Cho, Y. H. Kim, S. J. Jeong, S. Park, H. J. Lee, H. Kim, *ACS Appl. Mater. Interfaces* **2016**, *8*, 8576.
[44] L. Li, S. Ye, J. Qu, F. Zhou, J. Song, G. Shen, *Small* **2021**, *17*, e2005606.
[45] L. Dou, Y. Yang, J. You, Z. Hong, W.-H. Chang, G. Li, Y. Yang, *Nat. Commun.* **2014**, *5*, 5404.
[46] F.-X. Liang, J.-Z. Wang, Z.-X. Zhang, Y.-Y. Wang, Y. Gao, L.-B. Luo, *Adv. Opt. Mater.* **2017**, *5*, 1700654.
[47] D. Han, K. Liu, X. Chen, B. Li, T. Zhai, L. Liu, D. Shen, *Appl. Phys. Lett.* **2021**, *118*, 251101.
[48] W. Peng, X. Wang, R. Yu, Y. Dai, H. Zou, A. C. Wang, Y. He, Z. L. Wang, *Adv. Mater.* **2017**, *29*, 106698.
[49] H. Xia, M. Luo, W. Wang, H. Wang, T. Li, Z. Wang, H. Xu, Y. Chen, Y. Zhou, F. Wang, R. Xie, P. Wang, W. Hu, W. Lu, *Light Sci Appl* **2022**, *11*, 170.
[50] M. Moun, M. Kumar, M. Garg, R. Pathak, R. Singh, *Sci. Rep.* **2018**, *8*, 11799.
[51] Y. Cai, K. Zhang, Q. Feng, Y. Zuo, Z. Hu, Z. Feng, H. Zhou, X. Lu, C. Zhang, W. Tang, J. Zhang, Y. Hao, *Opt. Mater. Express* **2018**, *8*, 3506.
[52] H. Liu, X. Zhu, X. Sun, C. Zhu, W. Huang, X. Zhang, B. Zheng, Z. Zou, Z. Luo, X. Wang, D. Li, A. Pan, *ACS Nano* **2019**, *13*, 13573.
[53] A. Pezeshki, S. H. Shokouh, T. Nazari, K. Oh, S. Im, *Adv. Mater.* **2016**, *28*, 3216.
[54] M. Long, Y. Wang, P. Wang, X. Zhou, H. Xia, C. Luo, S. Huang, G. Zhang, H. Yan, Z. Fan, X. Wu, X. Chen, W. Lu, W. Hu, *ACS Nano* **2019**, *13*, 2511.
[55] Y. Tu, Y. Xu, J. Li, Q. Hao, X. Liu, D. Qi, C. Bao, T. He, F. Gao, W. Zhang, *Small* **2020**, *16*, 2005626.
[56] A. Islam, J. Lee, P. X. L. Feng, *ACS Photonics* **2018**, *5*, 2693.
[57] M. Dai, H. Chen, F. Wang, M. Long, H. Shang, Y. Hu, W. Li, C. Ge, J. Zhang, T. Zhai, Y. Fu, P. Hu, *ACS Nano* **2020**, *14*, 9098.
[58] W. Deng, Z. Zheng, J. Li, R. Zhou, X. Chen, D. Zhang, Y. Lu, C. Wang, C. You, S. Li, L. Sun, Y. Wu, X. Li, B. An, Z. Liu, Q. J. Wang, X. Duan, Y. Zhang, *Nat. Commun.* **2022**, *13*, 4627.